

# Real-time monitoring of polarization state deviations with dielectric metasurfaces

Shaun Lung<sup>Ⓧ</sup>,<sup>a</sup> Jihua Zhang<sup>Ⓧ</sup>,<sup>a,\*</sup> Kai Wang,<sup>b</sup> and Andrey A. Sukhorukov<sup>Ⓧ</sup><sup>a</sup>

<sup>a</sup>The Australian National University, Research School of Physics, Centre of Excellence for Transformative Meta-Optical Systems (TMOS), Department of Electronic Materials Engineering, Canberra, Australian Capital Territory, Australia

<sup>b</sup>McGill University, Department of Physics, Montréal, Quebec, Canada

**Abstract.** We propose and experimentally demonstrate a dielectric metasurface that allows monitoring of polarization deviations from an arbitrary elliptical input anchor state simply by tracking in real-time the output ratio between the powers of horizontal and vertical components after the metasurface. Importantly, this ratio can be enhanced corresponding to increased responsivity. Such nontrivial functionality is achieved by designing binary metasurfaces that realize tailored nonunitary and chiral polarization transformation. We experimentally demonstrate the operation at telecommunication wavelengths with enhanced responsivity up to 25 for various anchor states, including the strongly elliptical and circular. We also achieve the uncertainty of deviation measurement that is significantly better than the fundamental limit for nonchiral metasurfaces.

Keywords: nanophotonics; metasurface; polarimetry; nanostructure; nanofabrication.

Received Oct. 12, 2022; revised manuscript received Nov. 26, 2022; accepted for publication Dec. 31, 2022; published online Feb. 2, 2023.

© The Authors. Published by SPIE and CLP under a Creative Commons Attribution 4.0 International License. Distribution or reproduction of this work in whole or in part requires full attribution of the original publication, including its DOI.

[DOI: [10.1117/1.APN.2.2.026003](https://doi.org/10.1117/1.APN.2.2.026003)]

## 1 Introduction

Measurement of polarization and monitoring its change are enabling factors to versatile applications including universe exploration,<sup>1</sup> seismic sensing,<sup>2</sup> optical biopsy,<sup>3,4</sup> quantum optics,<sup>5,6</sup> material characterization,<sup>7</sup> and so on. This is done by an instrument called a polarimeter, which typically contains a tunable phase retarder followed by a polarizer.<sup>8</sup> By adjusting the orientation or phase retardance of the phase retarder multiple times and recording the output powers, the four Stokes parameters of the input state can be retrieved.<sup>9</sup> However, the requirement for multiple reconfigurable optical elements and several measurements makes this scheme bulky and limits the temporal resolution.

In the last decade, metasurfaces comprising a thin layer of nanostructures have shown exceptional capabilities in the manipulation of both classical<sup>10,11</sup> and quantum<sup>12–14</sup> light associated with the polarization degree of freedom. Metasurfaces have enabled single-shot polarization measurements in a compact integrated form, without a need for reconfigurability, by dividing

the beam into multiple spatial paths.<sup>13,15–19</sup> However, these metasurface polarimeters still require computational data processing to reconstruct the input state from several output power measurements, placing a fundamental restriction on the measurement speed. This poses a scientific and practical question on the potential for metasurfaces to facilitate direct monitoring of polarization states, which would boost the application of meta-optics for sensitive detection that is relevant to multiple aspects of polarization optics.

We develop and experimentally demonstrate a monolithic dielectric metasurface for real-time monitoring with enhanced responsivity of small deviations in the vicinity of arbitrarily chosen linear, circular, and general elliptical polarization states. We draw on the concepts of nonunitary transformations that can enable the enhancement of small polarization differences and transform two adjacent polarization states on the Poincaré sphere into orthogonal ones.<sup>20,21</sup> With nonunitary metasurface transformations proven for polarization pair transformation, we now present a novel scheme for metasurfaces utilizing tailored and nonunitary polarization transformations to monitor small polarization changes. Notably, this scheme is simple to implement, requiring only the measurement of the intensities

\*Address all correspondence to Jihua Zhang, [jhzhanghust@gmail.com](mailto:jhzhanghust@gmail.com)

of horizontal and vertical polarization outputs. Here, we suggest a more general approach, where the anchor state and any perturbations around it are transformed by the metasurface to the output linear polarizations, for example, the vertical and horizontal ones, respectively. Then, the magnitude of perturbations can be directly monitored simply by tracking the ratio of detected powers for the two output linear polarizations, without any substantial computational processing. Importantly, this ratio can be enhanced through judicious design to aid the monitoring of weak polarization deviations, where such increased responsivity is achieved through a tailored nonunitary metasurface transformation. We present a general theory and experimentally demonstrate monitoring of small polarization deviations around a highly elliptical state and a near-circular polarization state, with the responsivity reaching values of over an order-of-magnitude enhancement. We also predict and confirm through measurements that chiral response can be attained to a useful degree using the simple binary pixel concept of our metasurfaces.

## 2 Theoretical Concept

We schematically show the concept of the metasurface-enabled sensitive monitoring of polarization deviations in Fig. 1. An arbitrarily chosen linear, circular, or elliptical anchor polarization state denoted as  $|\psi\rangle$  is shown by a red cross on the Poincaré sphere in Fig. 1(a). We aim to detect the presence of perturbations that alter the anchor polarization, which can be denoted as  $\delta|\psi_{\perp}\rangle$ . Here,  $\delta$  is a small complex-valued deviation magnitude, and by definition, we consider the perturbations that are orthogonal to the anchor state, such that  $\langle\psi_{\perp}|\psi\rangle \equiv 0$ , and we assume the normalization  $\langle\psi_{\perp}|\psi_{\perp}\rangle = \langle\psi|\psi\rangle = 1$ . In the figure, the spherical crown around the anchor polarization marks a range of the perturbed input states, with the color indicating the squared magnitude of the deviations up to  $|\delta|^2 \leq 0.01$ . Defining the output polarization state after the metasurface as  $|\psi_{\text{out}}\rangle = T|\psi_{\text{in}}\rangle = \xi(|V\rangle + \alpha\delta|H\rangle)$ , we show that direct monitoring of polarization perturbations with increased responsivity can be accomplished using the following polarization transformation:

$$T = \xi(|V\rangle\langle\psi| + \alpha|H\rangle\langle\psi_{\perp}|), \quad (1)$$

where  $|H\rangle$  and  $|V\rangle$  are the horizontal and vertical polarizations, respectively, and  $\alpha$  is a parameter quantifying the output enhancement of the initial deviation  $\delta$  relative to the anchor state. We see that the metasurface projects the anchor state  $|\psi\rangle$  to the output vertical linear polarization  $|V\rangle$  with a power transmittance  $|\xi|^2$ . On the other hand, a small deviation  $\delta|\psi_{\perp}\rangle$  is transformed to the output horizontal linear polarization  $|H\rangle$  with a power transmittance  $|\xi\alpha|^2$ . Then, the presence of input polarization deviations can be directly detected by simply splitting the output horizontal and vertical components and monitoring the ratio of their respective powers  $P_{H,V}$ , which is directly proportional to the magnitude of the input perturbations  $P_H/P_V = |\alpha|^2|\delta|^2$ . Experimentally, such measurement can be straightforwardly implemented with a single polarizing beam splitter and two detectors, as sketched in Fig. 1(b). We also define the responsivity of the detection as  $\eta = |\alpha|^2$ , wherein larger values facilitate stronger variations in the output polarization state and specifically the ratio  $P_H/P_V$ , even for small perturbation amplitudes; see Fig. 1(c). After measuring the output  $P_H/P_V$ , and knowing the responsivity value  $\eta$  of the metasurface, the amplitude of the input deviation can be directly obtained as  $|\delta| = \sqrt{(P_H/P_V)/\eta}$ .

## 3 Effects of Chirality on Polarization Sensing

It is also essential to consider the degree of uncertainty in determining the magnitude of deviations from the anchor state under practical conditions. We show in the following that, for our measurement scheme, this uncertainty is fundamentally limited by the chiral degree of freedom attainable by the metasurface. Indeed, we note that the ideal transformation in Eq. (1) is in general nonunitary and chiral, particularly for highly elliptical and circular anchor polarization states. In practice, the transformation enabled by dielectric metasurfaces at normal incidence typically has weak chirality. Yet the absence of material absorption in dielectric structures is beneficial for the manipulation of classical and especially quantum<sup>22,23</sup> light. Importantly, we find that metasurfaces with no or limited chirality can always implement the following transformation, which allows for the monitoring of polarization deviations according to our concept,

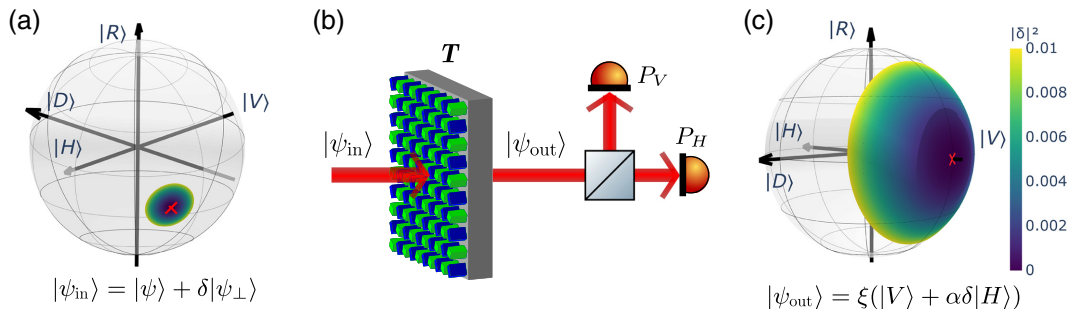


**Fig. 1** Concept of polarization monitoring with a metasurface. (a) An arbitrarily chosen elliptical anchor polarization (red cross) on a Poincaré sphere and deviations  $|\delta|^2$  up to 0.01 are indicated by a crown. (b) An experimental scheme utilizing a metasurface performing a special nonunitary transformation  $T$  that maps a perturbed input polarization  $|\psi_{\text{in}}\rangle$  to an output state  $|\psi_{\text{out}}\rangle$ , allowing for real-time monitoring of input polarization deviations using only a polarizing beam splitter and the power measurements  $P_V$  and  $P_H$ . (c) At the output, the anchor state is converted to the vertical polarization, and the horizontal component represents the deviation, which is enhanced by a responsivity factor  $\eta$ .

$$T = \xi(|V\rangle\langle\psi| + \alpha|H\rangle\langle\psi_{\perp}| + \gamma|V\rangle\langle\psi_{\perp}|). \quad (2)$$

We define here an extension to Eq. (1) with an additional complex variable  $\gamma$ . The introduced additional term thus quantifies the portion of the input deviation that is mapped to the  $|V\rangle$  state instead of the desired  $|H\rangle$  state, which may be unavoidable for practical metasurface designs. Then, the output power ratio becomes

$$\sqrt{(P_H/P_V)/\eta} = |\delta|/|1 + \gamma\delta|. \quad (3)$$

Importantly, the nonzero values would indicate a presence of polarization deviations, according to our operating principle, shown in Fig. 1. We may also notice from the extended form of Eq. (3) that there exists a relative uncertainty with which one can determine the amplitude of initial deviation after measuring the output power ratio:

$$|\delta| \in [\sqrt{(P_H/P_V)/\eta} - |\gamma|(P_H/P_V)/\eta, \sqrt{(P_H/P_V)/\eta} + |\gamma|(P_H/P_V)/\eta]. \quad (4)$$

A more detailed derivation may be found in Sec. S4 in the [Supplementary Material](#). Accordingly, the uncertainty range can be estimated as  $2|\gamma|(P_H/P_V)/\eta \approx 2|\gamma||\delta|^2$ , denoting a relative uncertainty of  $2|\gamma\delta|$  to the initial deviation. In general, this arises from the fact that the phase information of the input polarization states is discarded. Consequently, any given value of  $P_H/P_V$  corresponds to a range of complex  $\delta$  values wherein only the real value  $|\delta|$  is captured by the measurement. Accordingly, this degree of uncertainty may be controlled to maximize the accuracy of measurement by adding a secondary design goal in the form of minimizing the fraction of perturbation power mapped to the  $|V\rangle$  component at the output, i.e.,  $|\gamma|^2$ .

For comparison, we analytically derived the Jones matrix required for a nonchiral, nonamplifying metasurface that fits the constraints of this transformation. From this analysis, we find that the optimal symmetrical transfer matrix  $T$  for the anchor state  $[\cos \beta, \sin \beta e^{i\varphi}]^T$  and a target responsivity  $\eta_0$  is

$$T = \frac{1}{\sigma_{\max}} \begin{bmatrix} -\sin \beta e^{i\varphi} & \cos \beta \\ \cos \beta & \frac{1/\sqrt{\eta_0} - \cos^2 \beta}{\sin \beta} e^{-i\varphi} \end{bmatrix}, \quad (5)$$

where  $\sigma_{\max}$  is the maximum singular value of the matrix expression in brackets. The details, along with the full derivation of Eq. (5), are provided in Sec. S1 in the [Supplementary Material](#). We use Eq. (5) to calculate the corresponding value of  $\gamma_{\text{sym}}$ , which defines a fundamental minimal limit for the  $\gamma$  value that applies when the metasurface has no chirality whatsoever:

$$|\gamma| \geq |\gamma_{\text{sym}}| = \min\{\tan \beta, \cot \beta\}(\sqrt{\eta_0} - 1). \quad (6)$$

Importantly, by designing a metasurface with specific chiral response, one can achieve smaller  $\gamma$ , overcoming the limit in Eq. (6), and thereby attain a higher degree of precision in determining the deviations from the anchor state. We demonstrate such chiral metasurface advantage experimentally in the following section.

## 4 Metasurface Experimental Realization

We achieve the required nonunitary transformation  $T$  with a monolithic dielectric metasurface by nontrivially generalizing the use of binary structures, which were previously developed for polarization pair transformations.<sup>21</sup> Figure 2(a) shows one unit cell of the binary metasurface, which comprises two types of silicon nanopillars, each having a different dimension and orientation angle. The period of the metasurface is designed to be larger than that of the operating wavelength such that the metasurface supports multiple diffraction orders in the transmission. We note that while the subpixels will be spaced at a periodicity much less than one wavelength, the  $2 \times 2$  supercell as a whole can exceed the wavelength of incident light. The metasurface is tailored to realize the targeted polarization transformation in the zero-order transmission. Specifically, the metasurface transforms the anchor state  $|\psi\rangle$  into  $|V\rangle$  in the zero order with a designer reduction of power, where the attenuation is in the form of diffraction, as shown in Fig. 2(b). Input perturbations  $|\psi_{\perp}\rangle$  that are orthogonal to the anchor state are transformed by the metasurface into the horizontal polarization state  $|H\rangle$  in the zeroth order with nearly maximum transmissivity, since we aim to minimize the diffraction for such states, as shown in Fig. 2(c).

Note that different from previous work, here we extend the capability of the binary metasurface for realizing chiral polarization transformations by numerically optimizing the geometric

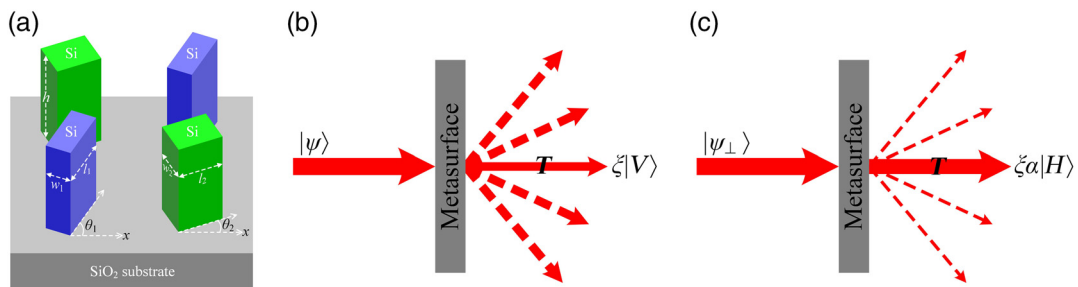


**Fig. 2** Schematic representation of optimal metasurface for monitoring of polarization deviations. (a) One unit cell of the silicon metasurface for achieving the nonunitary transformation  $T$ . Response of metasurface to incident (b) anchor polarization state  $|\psi\rangle$  and (c) perturbed state  $|\psi_{\perp}\rangle$ . The diffraction losses are specially designed to be stronger or weaker, as shown by thicker or thinner dashed lines, respectively.

parameters of the unit cell. Specifically, for a given anchor polarization state and a target responsivity, we experimentally achieve a chiral  $T$  as close as possible to the ideal one in Eq. (1) with minimal deviation. It should be noted that attaining strong intrinsic chirality in a dielectric metasurface is a nontrivial task<sup>24,25</sup> that we accomplish via numerical optimization techniques. In this work, this was achieved by tuning the design space of the metasurface, including the period of the unit cell, and the dimensions ( $l_{1,2}$  and  $w_{1,2}$ ) and orientation angles ( $\theta_{1,2}$ ) of the two nanopillars, optimizing for the similarity of the Jones matrix to the ideal one given by Eq. (1). An additional degree of freedom is provided by the overall orientation of the metasurface (defined as  $\theta$ ), which is further tunable under experimental conditions. While the structures are fabricated in a two-by-two square lattice, the metasurface may be rotated around the axis of the incident laser, providing extra and significant control over its polarization manipulation behavior. The primary simulation tool used to accomplish this is a rigorous coupled-wave analysis solver, a mature and extensively developed algorithm for semi-analytical computation of electromagnetic wave equations.<sup>26,27</sup> With this controllability, we designed a binary metasurface that can perform sensitive deviation measurement near two polarization states, one highly elliptical and one near-circular polarization state, in the near-infrared telecommunication wavelength band. The specific dimension parameters are the unit cell period of 1800 nm,  $l_1 = 735.9$  nm,  $w_1 = 274$  nm,  $\theta_1 = 52.86$  deg;  $l_2 = 395.3$  nm,  $w_2 = 256.8$  nm,  $\theta_2 = 173.52$  deg, and  $h = 800$  nm. Whereas a detailed investigation of the optical chirality origins in our metasurface is beyond the scope of this work, we note that chirality in the dielectric metasurfaces can arise from two primary mechanisms: the coupling between nanopillars<sup>28</sup> and substrate-induced asymmetry along the propagation direction.<sup>29</sup> Further numerical simulations were also performed to test for the robustness of the metasurface design against variations in the subpixel size that might arise from fabrication, and are shown in Sec. S5 in the [Supplementary Material](#).

The designed silicon metasurface is then fabricated in the cleanroom through the following nanofabrication procedures. We start from a glass substrate with a thickness of 160  $\mu\text{m}$ . After cleaning, a 832 nm layer of amorphous silicon is deposited onto the substrate by using plasma-enhanced chemical vapor deposition. Following that, bilayer polymethyl methacrylate (PMMA) is spin-coated as the photoresist for electron beam lithography. Then, 70 nm thick aluminum is deposited by the electron beam deposition technique, followed by a lift-off process to define the designed nanopattern. The designed nanopattern is transferred to the amorphous silicon layer by inductively coupled plasma etching by applying the aluminum nanostructures as the hard mask. Finally, the aluminum hard mask is removed by chemical etching. Figure 3(a) depicts the scanning electron image of the fabricated metasurface.

The polarization transformation matrix in the Jones formalism of the fabricated metasurface in the zero transmission order was then characterized in free space. Polarization states were prepared by a sequential set of polarizer, half-wave plate, and quarter-wave plate. The prepared polarization state is projected through the metasurface, and finally, the transmitted state is measured using a quarter-wave plate and a stationary polarizer. This allowed for full characterization of the transfer matrices  $T$  of the metasurface across a range of wavelengths;<sup>21</sup> further details may be found in Sec. S2 in the [Supplementary Material](#). Figures 3(b)–3(f) show experimental results of fabricated

metasurfaces. Figure 3(b) shows the characterized Jones matrix of the metasurface at 1573.8 nm with a rotation angle of  $\theta = 64$  deg. Note that this matrix is nonunitary and chiral, as desired in this work, with eigenvectors

$$\mathbf{v}_1 = \begin{bmatrix} 0.996 \\ 0.009 - 0.0278i \end{bmatrix}, \mathbf{v}_2 = \begin{bmatrix} 0.1268 + 0.3258i \\ 0.9369 \end{bmatrix}.$$

The corresponding anchor state has a Jones vector  $[\cos(0.362\pi), \sin(0.362\pi) \exp(-0.390\pi i)]^T$ . This is a highly elliptical state, as indicated by the red cross on the Poincaré sphere in Fig. 3(b), which shows the anchor states as a function of the metasurface rotation angle in the range from  $-90$  deg to  $90$  deg. Clearly, one can use the single metasurface to function for different anchor states in a big range on the Poincaré sphere by simply rotating the metasurface. And this range can be further doubled by mapping the anchor state to the  $|H\rangle$  and the deviation state to the  $|V\rangle$  (see detailed results in Sec. S4 in the [Supplementary Material](#)).

Featuring the transfer matrix in Fig. 3(b), the metasurface supports sensitive monitoring of polarization deviations near the anchor state with a responsivity up to 25, which is qualified by the slope of output  $H - V$  power ratio versus the input power of the deviations  $|\delta|^2$ , as shown in Fig. 3(d). A certain  $P_H/P_V$  can correspond to a range of deviation magnitudes, which results in an uncertainty of determining  $|\delta|$ . However, we emphasize that this relative uncertainty is on the order of  $2|\gamma\delta|$ , as we have discussed in Sec. 3. It scales with the magnitude of the perturbation  $\delta$ . This facilitates accurate monitoring of ultrasmall deviations.

The responsivity as a function of the metasurface rotation angle is shown in Fig. 3(e). One can see that it is maximized near the rotation angle we discussed above in Figs. 3(b) and 3(d), as indicated by the vertical dashed line. The  $|\gamma|$  value also reaches the smallest value of 0.646 near this angle, as shown by the solid line in Fig. 3(f). This corresponds to a relative uncertainty of  $1.292|\delta|$ , or about 12.9% when the deviation magnitude is 10% of the input anchor state. For comparison, the smallest  $|\gamma_{\text{sym}}|$  achievable in case of a symmetrical (i.e., nonchiral) transfer matrix for the same anchor state and responsivity is also shown in Fig. 3(f) by the dashed line. We can see that in the shaded region, our fabricated chiral metasurface has superior polarization discrimination as compared to any symmetrical one. This lower degree of uncertainty allows sensitive deviation monitoring. We also observe that the value of  $\eta$  decreases as we depart from the designed angle, which happens because a larger portion of the transmitted light is no longer transferred to the intended polarization outputs.

Next, at the optimized rotation angle  $\theta = 64$  deg, we directly measured the output  $H - V$  power ratios after the metasurface when varying the input deviations from the anchor state. The black line and blue shaded region in Fig. 4(a) show the polarization ellipse of the anchor state and perturbed polarization ellipse range for deviations with the magnitude up to  $|\delta| = 0.1$ . For each perturbed input state, we measure the output  $H - V$  power ratio and plot them at the corresponding point on the Poincaré sphere in Fig. 4(b). As can be seen, the ratio is minimized at the anchor state and increases proportionally with the deviation magnitude. We also represent these measurement data versus the squared deviation magnitude in Fig. 4(c), where the color of the data points represents the phase of the input deviation  $\phi_\delta$  and determines the responsivity value of

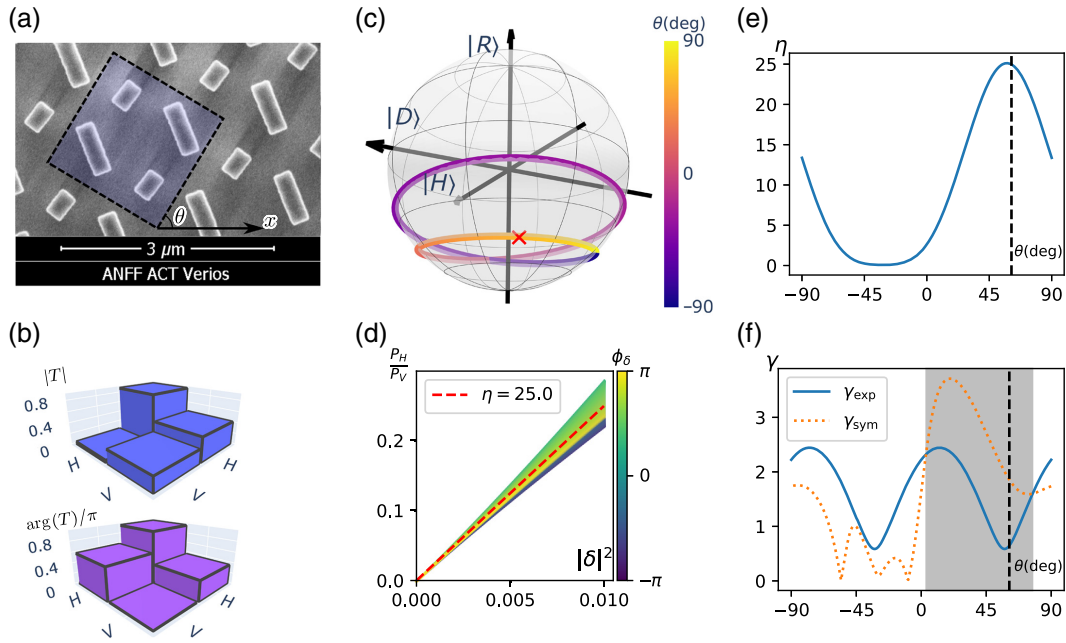


**Fig. 3** (a) Scanning electron microscope (SEM) image of metasurface fabricated to implement polarization sensing. The unit cell is indicated using the black, dashed box, with rotation from the horizontal indicated by  $\theta$ . (b) Experimentally characterized transfer matrix of the metasurface at  $\theta = 64$  deg. (c) Dependence of the anchor state on the metasurface rotation angle  $\theta$  displayed on a Poincaré sphere, with  $|D\rangle$ ,  $|H\rangle$ , and  $|R\rangle$  indicating the diagonal, horizontal, and right-circular polarization states, respectively. The anchor state relating to the transfer matrix in (b) is indicated by the red cross. (d) Predicted power ratios  $P_H/P_V$  against deviation from anchor state  $|\delta|^2$ . The phase of the deviation  $\phi_\delta$ , indicated by the color gradient, results in a relative uncertainty range  $2|\gamma\delta|$  in determining  $|\delta|$ . (e) Variation of responsivity as the metasurface is rotated by angle  $\theta$ . The angle corresponding to (b) and (d) is indicated by the dashed line. (f) Uncertainty parameter  $|\gamma_{\text{exp}}|$  dependence on the rotation of the metasurface. Shown for comparison is a theoretically best value  $|\gamma_{\text{sym}}|$  for any nonchiral metasurface with purely symmetrical transfer matrix, considered for the same anchor state and responsivity. Shading indicates the region with  $|\gamma_{\text{exp}}| < |\gamma_{\text{sym}}|$ , where experimental results demonstrate the advantage of the chiral response. Details of these calculations can be found in Sec. S3 in the [Supplementary Material](#).

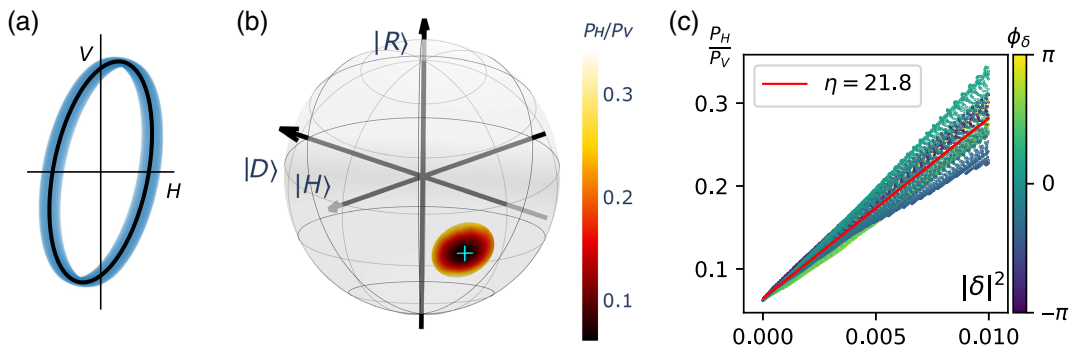


**Fig. 4** Experimental measurement of power ratios for an elliptical anchor state of  $[\cos(0.362\pi), \sin(0.362\pi) \exp(-0.390\pi i)]^T$ , for the metasurface rotated at an angle  $\theta = 64$  deg and operating wavelength of 1573.8 nm. (a) The polarization ellipse of the input polarization states used for the measurement. The precise anchor state is indicated by the black line, with variations from this state indicated by the blue, shaded region. (b) Measured output power ratios ( $P_H/P_V$ ) plotted on a Poincaré sphere with positions corresponding to the corresponding input polarization states. The color shading indicates the variation of power ratio as the state deviates from the anchor state (cyan marker). (c) The experimental power ratios plotted versus the deviations from the anchor states.

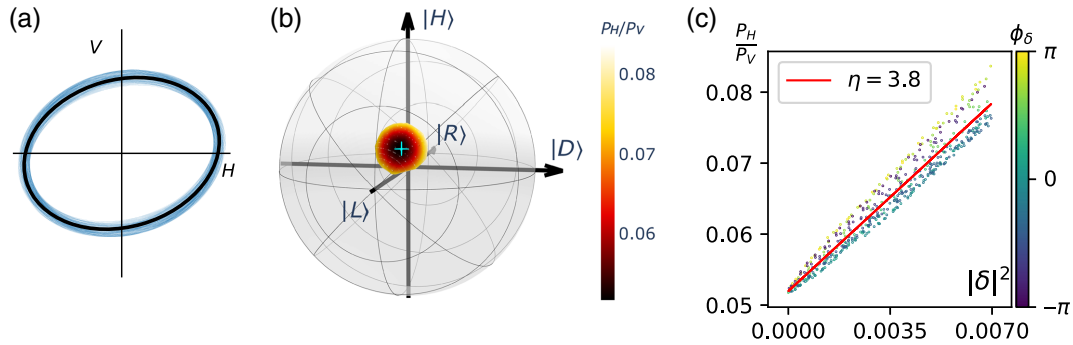


**Fig. 5** Experimental results for a near-circular anchor state of  $[\cos(0.21\pi), \sin(0.21\pi) \exp(-0.448\pi i)]^T$ , for the metasurface rotated at an angle  $\theta = -58$  deg and operating wavelength of 1550.5 nm. Plots (a)–(c) follow the same conventions as in Fig. 4.

$\eta = 21.8$ . The demonstrated responsivity is slightly smaller than the predicted value from the characterized transfer matrix in Fig. 3(b). There are several possible factors contributing to this overall discrepancy: the numerical fitting error of the algorithm in reconstruction of the transfer matrix, mechanical rotation error of the wave plates, dependence of the transfer matrix on the incident angle, nonuniformity of the metasurface, and transverse beam shift when the polarizers and wave plates are at different orientations. We anticipate that these technical issues can be mitigated through improved experimental implementations. Importantly, despite such detrimental experimental factors, the metasurface operation successfully showcases that the theoretical concepts constitute reliable design principles that may be utilized for practical measurements. Based on the maximum and minimum values of  $|\delta|$  (i.e., the uncertainty of measuring  $|\delta|$ ) for a certain  $H$ - $V$  power ratio, we determine the experimental  $|\gamma|$  to be 1.33. Although it is larger than the predicted value from the characterized transfer matrix ( $|\gamma| = 0.646$ ), it is still smaller than the theoretical best value ( $|\gamma_{\text{sym}}| = 1.826$ ) for a symmetrical transfer matrix as shown in Fig. 3(f), confirming the advantage of specific chiral metasurface response achieved experimentally.

Lastly, we further demonstrated the proposed concept for an anchor state close to the right circular polarization by rotating the same metasurface at a different angle  $\theta = -58$  deg and operating it at a wavelength of 1550.5 nm. The corresponding results are presented in Fig. 5. The anchor state has a Jones vector  $[\cos(0.21\pi), \sin(0.21\pi) \exp(-0.448\pi i)]^T$ , whose polarization ellipse is indicated by the black line in Fig. 5(a) and whose position on Poincaré sphere is marked by the cyan cross in Fig. 5(b). Based on a representation in Fig. 5(c), for this anchor state we determine the experimental responsivity of  $\eta = 3.8$ . Note that it is more difficult to achieve a high responsivity for a circular anchor state as compared with an elliptical one as a result of the more stringent requirement on the chirality of the transformation in Eq. (1). For this near-circular anchor state, the experimentally measured  $|\gamma|$  is 0.815. Importantly, it is below the theoretical best value for a symmetrical transfer matrix of  $|\gamma_{\text{sym}}|$ , which is 1.224 for the same anchor state and responsivity.

We anticipate that higher responsivity for circular states might be achieved in the regime of an angular incidence to the metasurface, as in this case the chiral response may be enhanced even further via the use of extrinsic chirality.<sup>30</sup>

## 5 Conclusions

We reveal that dielectric metasurfaces can provide enhanced responsivity for monitoring small deviations around an arbitrarily chosen anchor polarization state through a simple readout of output horizontal and vertical component powers. We formulate a metasurface design principle and fabricate metasurfaces with a specially optimized binary combination of nanoresonators. The experimental measurements demonstrate high responsivity and precision in monitoring deviations around elliptical and circular input states.

While the metasurface demonstrated in this paper was optimized for the telecommunication wavelength band, the fundamental design principles are flexible and extensible to other wavelengths. In particular, at visible wavelengths where silicon exhibits higher absorption, the metasurface design can be based on other dielectric materials (such as titanium dioxide<sup>31,32</sup>). On the other hand, given that the target measurement after the metasurface is the power ratio of horizontal and vertical polarizations, the metasurface can potentially perform the required polarization transformations even in presence of material losses, although the signal-to-noise ratio would be reduced.

We also show that the monitored state can be adjusted by rotating the metasurface. In the future, tilting the metasurface could serve as additional possibility to tune the polarization transformations.<sup>33</sup> Furthermore, one can also employ various physical mechanisms to tune the metasurface transmission,<sup>34</sup> for example, using liquid crystals<sup>35</sup> or phase-change materials in combination with quasi-bound state in continuum (quasi-BIC) resonances.<sup>36,37</sup>

We anticipate that our work will support the development of a new class of ultracompact and ultrasensitive flat meta-optical devices for a broad range of applications, including advanced sensing, imaging, and metrology in both classical and quantum photonics.

## Acknowledgments

The authors would like to thank Dragomir Neshev, Mohsen Rahmani, and Khosro Zangeneh Kamali for insightful discussions and comments. This work was supported by the Australian Research Council (Grant Nos. NI210100072 and CE200100010) and US AOARD (Grant No. 19IOA053). The metasurface fabrication was performed at the Australian National University node of the Australian National Fabrication Facility (ANFF),

a company established under the National Collaborative Research Infrastructure Strategy to provide nano- and microfabrication facilities for Australia's researchers. The authors declare no conflicts of interest.

### Code, Data, and Materials Availability

Data underlying the results presented in this paper may be obtained from the authors upon reasonable request.

### References

1. Y. Minami and E. Komatsu, "New extraction of the cosmic birefringence from the Planck 2018 polarization data," *Phys. Rev. Lett.* **125**, 221301 (2020).
2. Z. W. Zhan et al., "Optical polarization-based seismic and water wave sensing on transoceanic cables," *Science* **371**, 931–936 (2021).
3. M. R. Antonelli et al., "Mueller matrix imaging of human colon tissue for cancer diagnostics: how Monte Carlo modeling can help in the interpretation of experimental data," *Opt. Express* **18**, 10200–10208 (2010).
4. M. Duda et al., "Polarization of myosin II refines tissue material properties to buffer mechanical stress," *Dev. Cell* **48**, 245–260 (2019).
5. D. F. V. James et al., "Measurement of qubits," *Phys. Rev. A* **64**, 052312 (2001).
6. H. Z. Liu et al., "Enhanced high-harmonic generation from an all-dielectric metasurface," *Nat. Phys.* **14**, 1006–1010 (2018).
7. H. G. Tompkins and J. N. Hilfiker, *Spectroscopic Ellipsometry: Practical Application to Thin Film Characterization*, Momentum Press (2015).
8. H. G. Berry, G. Gabrielse, and A. E. Livingston, "Measurement of Stokes parameters of light," *Appl. Opt.* **16**, 3200–3205 (1977).
9. M. Chekhova and P. Banzer, *Polarization of Light in Classical, Quantum, and Nonlinear Optics*, De Gruyter, Berlin (2021).
10. N. F. Yu and F. Capasso, "Flat optics with designer metasurfaces," *Nat. Mater.* **13**, 139–150 (2014).
11. Y. Q. Hu et al., "All-dielectric metasurfaces for polarization manipulation: principles and emerging applications," *Nanophotonics* **9**, 3755–3780 (2020).
12. T. Stav et al., "Quantum entanglement of the spin and orbital angular momentum of photons using metamaterials," *Science* **361**, 1101–1104 (2018).
13. K. Wang et al., "Quantum metasurface for multiphoton interference and state reconstruction," *Science* **361**, 1104–1108 (2018).
14. C. L. Zheng et al., "All-dielectric metasurface for manipulating the superpositions of orbital angular momentum via spin-decoupling," *Adv. Opt. Mater.* **9**, 2002007 (2021).
15. A. Pors, M. G. Nielsen, and S. I. Bozhevolnyi, "Plasmonic meta-gratings for simultaneous determination of Stokes parameters," *Optica* **2**, 716–723 (2015).
16. J. P. B. Mueller, K. Leosson, and F. Capasso, "Ultracompact metasurface in-line polarimeter," *Optica* **3**, 42–47 (2016).
17. E. Arbabi et al., "Full-Stokes imaging polarimetry using dielectric metasurfaces," *ACS Photonics* **5**, 3132–3140 (2018).
18. Y. Intaravanne and X. Z. Chen, "Recent advances in optical metasurfaces for polarization detection and engineered polarization profiles," *Nanophotonics* **9**, 1003–1014 (2020).
19. Y. D. Shah et al., "An all-dielectric metasurface polarimeter," *ACS Photonics* **9**, 3245–3252 (2022).
20. A. Cerjan and S. H. Fan, "Achieving arbitrary control over pairs of polarization states using complex birefringent metamaterials," *Phys. Rev. Lett.* **118**, 253902 (2017).
21. S. Lung et al., "Complex-birefringent dielectric metasurfaces for arbitrary polarization-pair transformations," *ACS Photonics* **7**, 3015–3022 (2020).
22. A. Arbabi and A. Faraon, "Fundamental limits of ultrathin metasurfaces," *Sci. Rep.* **7**, 43722 (2017).
23. A. S. Solntsev, G. S. Agarwal, and Y. Y. Kivshar, "Metasurfaces for quantum photonics," *Nat. Photonics* **15**, 327–336 (2021).
24. S. V. Zhukovsky, A. V. Novitsky, and V. M. Galynsky, "Elliptical dichroism: operating principle of planar chiral metamaterials," *Opt. Lett.* **34**, 1988–1990 (2009).
25. L. A. Warning et al., "Nanophotonic approaches for chirality sensing," *ACS Nano* **15**, 15538–15566 (2021).
26. P. Lalanne, "Improved formulation of the coupled-wave method for two-dimensional gratings," *J. Opt. Soc. Am. A* **14**, 1592–1598 (1997).
27. M. M. R. Elsayy et al., "Numerical optimization methods for metasurfaces," *Laser Photonics Rev.* **14**, 1900445 (2020).
28. H. S. Khaliq et al., "Giant chiro-optical responses in multipolar-resonances-based single-layer dielectric metasurfaces," *Photonics Res.* **9**, 1667–1674 (2021).
29. S. Nechayev et al., "Substrate-induced chirality in an individual nanostructure," *ACS Photonics* **6**, 1876–1881 (2019).
30. J. Kim et al., "Chiroptical metasurfaces: principles, classification, and applications," *Sensors* **21**, 4381 (2021).
31. R. C. Devlin et al., "Broadband high-efficiency dielectric metasurfaces for the visible spectrum," *Proc. Natl. Acad. Sci. U. S. A.* **113**, 10473–10478 (2016).
32. A. Y. Zhu et al., "Giant intrinsic chiro-optical activity in planar dielectric nanostructures," *Light Sci. Appl.* **7**, 17158 (2018).
33. Z. J. Shi et al., "Continuous angle-tunable birefringence with free-form metasurfaces for arbitrary polarization conversion," *Sci. Adv.* **6**, eaba3367 (2020).
34. J. J. Hu et al., "Tunable nanophotonics," *Nanophotonics* **11**, 3741–3743 (2022).
35. A. Komar et al., "Dynamic beam switching by liquid crystal tunable dielectric metasurfaces," *ACS Photonics* **5**, 1742–1748 (2018).
36. A. Barreda et al., "Tuning and switching effects of quasi-BIC states combining phase change materials with all-dielectric metasurfaces," *Opt. Mater. Express* **12**, 3132–3142 (2022).
37. P. Moitra et al., "Programmable wavefront control in the visible spectrum using low-loss chalcogenide phase change metasurfaces," *Adv. Mater.*, 2205367 (2022).
38. Thorlabs, "WPH05M-1550 mounted multi-order wave plates, Part specification," (2022). [https://www.thorlabs.com/newgrouppage9.cfm?objectgroup\\_id=711](https://www.thorlabs.com/newgrouppage9.cfm?objectgroup_id=711) (accessed 17 November 2022).
39. J. Lekner, "Polarization of tightly focused laser beams," *J. Opt. A-Pure Appl. Opt.* **5**, 6 (2003).
40. N. H. Lindner and D. R. Terno, "The effect of focusing on polarization qubits," *J. Mod. Opt.* **52**, 1177–1188 (2005).

**Shaun Lung** received his doctorate degree from the Australian National University (ANU) in 2022, with a focus on polarization manipulation and measurement using metasurfaces, working primarily in experimental and computational aspects. He is working as a postdoctoral researcher at Friedrich Schiller Universität, Germany, in 2023. His interests remain within both computational and experimental optics, with a strong inclination toward metasurface development.

**Jihua Zhang** received his dual PhD from University Paris-Saclay and Huazhong University of Science and Technology in 2016. He is a research fellow in the Centre of Excellence for Transformative Meta-Optical Systems (TMOS) at the Research School of Physics of the ANU. Before joining TMOS, he was a postdoctoral associate at the Institute of Optics at University of Rochester. His current research is focused on nanostructured metasurfaces for nonlinear and quantum photonics.

**Kai Wang** received his PhD from the Australian National University in 2019. He is an assistant professor at McGill University and a chair in quantum photonics supported by the Ministère de l'Économie et de l'Innovation (MEI). Before joining McGill in 2023, he was a postdoc at

Stanford University. His research group focuses on the advanced manipulation of non-classical light for sensing and imaging applications and the emulation of fundamental physics using quantum photonic systems.

**Andrey A. Sukhorukov** is a professor at the Research School of Physics of the ANU and a member of the TMOS Centre. He leads a research

group on nonlinear and quantum photonics, targeting the fundamental aspects of the miniaturization of optical elements down to micro- and nanoscale. In 2015, he was elected Fellow of Optica for contributions to nonlinear and quantum integrated photonics, including frequency conversion and broadband light manipulation in waveguide circuits and metamaterials.